A GENERALIZED BIRKHOFF-ROTT EQUATION FOR 2D ACTIVE SCALAR PROBLEMS*

HUI SUN†, DAVID UMINSKY†, AND ANDREA L. BERTOZZI†

Abstract. In this paper we derive evolution equations for the 2D active scalar problem when the solution is supported on 1D curve(s). These equations are a generalization of the Birkhoff-Rott equation when vorticity is the active scalar. The formulation is Lagrangian and they are valid for nonlocal kernels K that may include both a gradient and an incompressible term. We develop a numerical method for implementing the model which achieves second order convergence in space and fourth order in time. We verify the model by simulating classic active scalar problems such as the vortex sheet problem (in the case of inviscid, incompressible flow) and the collapse of delta ring solutions (in the case of pure aggregation), finding excellent agreement. We then study two examples with kernels of *mixed type* - i.e., kernels that contain both incompressible and gradient flows. The first example is a vortex density model which arises in superfluids. We analyze the effect of the added gradient component on the Kelvin-Helmholtz instability. In the second example, we examine a nonlocal biological swarming model and study the dynamics of density rings which exhibit complicated milling behavior.

Key words. Birkhoff-Rott equation, active scalar problems, vortex density functions, Kelvin-Helmholtz instability, biological swarming.

AMS subject classifications. 76A25, 35B35, 37J25

1. Introduction.

The 2D active scalar problems we study in this paper take the form

$$\rho_t + \nabla \cdot (\rho \mathbf{v}) = 0, \qquad \rho(\mathbf{x}, 0) = \rho_0(\mathbf{x}), \tag{1.1}$$

$$\mathbf{v} = K * \rho = \nabla^\perp N * \rho + \nabla G * \rho \tag{1.2}$$

where $*$ denotes convolution, $(a, b)^\perp = (-b, a)$, and $\mathbf{x} \in \mathbb{R}^2$. Equations (1.1) - (1.2) represent a large class of problems which include fluids [23, 29, 11], chemotaxis [6], aggregation [4, 3, 17], biological swarming [31], and many others. Our work is focused on two facets of the 2D active scalar problem: First, we consider solutions supported on 1D curve(s); second, we look at the case when the velocity field contains both an incompressible and a gradient component. To better characterize the second motivation we assume sufficient smoothness and decay on K and apply the Hodge decomposition theorem [23] to the velocity field equation as expressed on the right hand side of equation (1.2). As such, the $\nabla^\perp N * \rho$ term represents the divergence-free or incompressible component of the velocity field and the $\nabla G * \rho$ is the gradient contribution to the velocity field. We refer to kernels K that contain both a divergence-free and a gradient part as kernels of *mixed type*.

Examples of mixed type kernels have been found in vortex models for superfluids, such as superconductors, where the active scalar is a "vortex density" function [7, 12, 22]. Classical 2D compressible fluids is another example in which K will have both an incompressible Newtonian potential and a compressible contribution (the dilatation) [13]. Mixed type kernels also arise in the work of Topaz and Bertozzi [31] in the context of kinematic social interaction models. They considered collective swarming motion kernels that contain both gradient and incompressible terms to better capture

*The work of DU was supported in part by DMS-0902792 and a UC President's fellowship. This work was also supported by NSF grants DMS-0907931 and EFRI - 1024765 and ONR grant N000141010641.

†UCLA Dept. of Mathematics, Box 951555, Los Angeles, CA 90095-1555

biological phenomena such as mill vortices and other rotating structures found in nature [16, 28, 26, 25].

There are many important examples when the kernel K creates a purely incompressible velocity field, i.e., $G = 0$. Such examples include quasi-geostrophic models [9, 10, 8] for which $N = (-\Delta)^{-\alpha}$ and, perhaps more famously, the vorticity formulation of the classical 2D Euler equations for which $N = \frac{1}{2\pi}\log|r|$ is the Biot-Savart kernel. Vorticity (the curl of the velocity field) is the active scalar in this second example and the well-studied problem known as the vortex sheet problem [14, 15, 21, 27] is the particular case when vorticity aggregates onto a 1D curve. It was first shown in [5] that the vortex sheet evolves according to the Birkhoff-Rott equation

$$\partial_t z(\Gamma, t) = \frac{1}{2\pi}\int_S \frac{(z(\Gamma,t) - z(\Gamma',t))^{\perp} \mathrm{d}\Gamma'}{|z(\Gamma,t) - z(\Gamma',t)|^2}, \tag{1.3}$$

where Γ is the local Lagrangian parameterization of the sheet S, and z is the position of the points on the sheet. The first goal of this paper is to derive an analogous equation to (1.3) for equations (1.1) - (1.2) where the kernel is general.

Examples of singular "sheet-like" solutions that occur for purely gradient kernels, i.e., $N = 0$, have been observed in chemotaxis models [16, 32] and purely aggregation kernels of the form $\nabla G(r) = \nabla|r|^{\alpha}$. Specifically, the analysis and dynamics of delta ring solutions has been studied in the works of Huang, Bertozzi, Laurent and others [17, 3, 4]. It has been shown that for $\alpha > 2$ smooth initial density may collapse to delta ring solutions in infinite time. For dimension two, finite time blow up "ring solutions" occur if $1 < \alpha < 2$. In this regime concentric density rings formally solve equations (1.1) - (1.2) and differential equations governing the radius of the rings can be computed; see [3]. Moreover if $\alpha > 2$ Huang et al. [18] have shown numerically that collapsing rings are attractors of radially symmetric solutions to equations (1.1)-(1.2).

Ring and curve solutions have also been discovered in biologically relevant attraction repulsion kernels such as $G(r) = \tanh((1-r)a) + b)$ and $G(r) = r^p - r^q$; see [19]. There, it was shown that certain parameter regimes for the above kernel have yielded linearly stable rings. In addition, low mode instabilities may develop - depending on parameters - where small perturbations of rings cause the ring to deform into a triangular-like closed curve. In addition, necessary and sufficient conditions were computed when a 1D curve is linearly well-posed.

In section 2 we derive a Lagrangian model using conservation of mass which is a generalization of the Birkhoff-Rott equation for vortex sheets and fully incorporates both incompressible and gradient velocity fields. In section 3 we define a numerical scheme for implementation and numerically show that it is second order accurate in space and fourth order accurate in time. In this section we also verify our model by simulating two well-studied problems: classic vortex sheet solutions and a purely aggregation model. In both the vortex sheet examples and the evolution of delta rings (in the case of the aggregation model) we obtain excellent agreement using our new model. In section 4 we first study a superfluids example which contains a kernel of mixed type. We observe that, by varying the weight of the incompressible versus gradient contribution to K, the maximal amount of vortex wind-up occurs when both pieces of the kernel are present (as opposed to just incompressible contributions). We explore this phenomenon by linearizing our solution and observe the effect the gradient term has on the associated Kelvin-Helmholtz instability. In our second example in section 4, we consider a swarming model and observe that (depending on parameters) the rotational contribution (N) to the kernel does not affect the contraction rate of

the curve but - somewhat surprisingly - the attractive, gradient contribution (G) to the kernel can have a very significant effect on the rotation dynamics of the curve. We conclude in section 5 with a discussion of directions and applications of this model to future research.

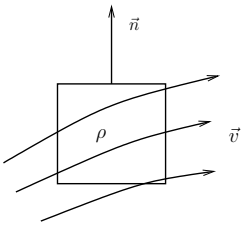

FIG. 2.1. *Schematic diagram of a box* ($\square$) *in a vector field.*

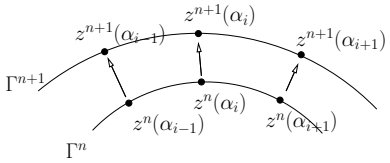

FIG. 2.2. *The evolution of the sheet from time* $n\Delta t$ *to* $(n+1)\Delta t$.

2. Derivation of density sheet equations. In this section we derive our model for the general active scalar problem for the case when all the mass concentrates on a 1D curve. We start our derivation by recalling that equation (1.1) is equivalent to conservation of mass. To see this, consider a small box $\square$ in the spatial domain as shown in Figure 2.1. Between time t and $t+\Delta t$, the amount of mass that flows out through the boundary of the box is approximately $\int_{\partial\square} \rho v n \mathrm{d}s\Delta t$, while the increase of the mass in the box is $\int_\square \rho \mathrm{d}x(t+\Delta t) - \int_\square \rho \mathrm{d}x(t)$. By conservation of mass, we arrive at the following equality:

$$\int_\square \rho \mathrm{d}x(t+\Delta t) - \int_\square \rho \mathrm{d}x(t) = \int_{\partial\square} \rho v n \mathrm{d}s\Delta t. \tag{2.1}$$

Dividing both sides by Δt and applying the divergence theorem, we get $\int_\square \rho_t \mathrm{d}x = \int_\square \nabla\cdot(\rho v)\mathrm{d}x$, and equation (1.1) follows.

For the case when all of the active scalar lies on a 1D curve - hereafter referred to as "the density sheet problem" - conservation of mass will be used to derive the equation of motion for the density sheet. To begin, let Γ^n be the sheet at time $n\Delta t$, and Γ^{n+1} be the sheet at time $(n+1)\Delta t$. We now parameterize our sheet, Γ, using an arbitrary Lagrangian parameter α; thus, we may write the position of the sheet as $z(\alpha) = (x(\alpha), y(\alpha)) \in \mathbb{R}^2$. Now choose α_{i-1}, α_i, and α_{i+1} to be three reference points on the density sheet, see 2.2.

The mass between α_{i-1} and α_{i+1} at time $n\Delta t$ is exactly $\int_{\alpha_{i-1}}^{\alpha_{i+1}} \rho|z_\alpha|(n\Delta t)\mathrm{d}\alpha$, while the mass between α_{i-1} and α_{i+1} at time $(n+1)\Delta t$ is $\int_{\alpha_{i-1}}^{\alpha_{i+1}} \rho|z_\alpha|((n+1)\Delta t)\mathrm{d}\alpha$. Since the reference points also move with the velocity field v, i.e.,

$$\frac{\partial z}{\partial t} = K * \rho, \tag{2.2}$$

the mass is conserved along trajectories for all time. This implies that

$$\int_{\alpha_{i-1}}^{\alpha_{i+1}} \rho|z_\alpha|(n\Delta t)\mathrm{d}\alpha - \int_{\alpha_{i-1}}^{\alpha_{i+1}} \rho|z_\alpha|((n+1)\Delta t)\mathrm{d}\alpha = 0 \tag{2.3}$$

where z_α denotes the derivative of z with respect to α. Dividing equation (2.3) by Δt, and letting $\Delta t \to 0$, we arrive at the following equation for the evolution of the

density ρ,

$$(\rho|z_\alpha|)_t = 0 \tag{2.4}$$

which may be written out as

$$\rho_t + \rho\frac{\langle z_\alpha, v_\alpha\rangle}{\langle z_\alpha, z_\alpha\rangle} = 0, \tag{2.5}$$

where $\langle\cdot,\cdot\rangle$ represent the usual inner product. Equations (2.5) and (2.2), or equivalently equations (2.4) and (2.2), yield a closed system of equations for the motion of the density sheet problem.

REMARK 2.1. *We note here that equations* (2.4) *and* (2.2) *represent a generalization of the Birkhoff-Rott equation* (1.3). *In particular if one chooses* N *to be the Newtonian potential and* $G = 0$, *equation* (2.4) *represents a parameterization with respect to circulation and thus* (2.2) *identically reduces to* (1.3). *Of course equations* (2.4) *and* (2.2) *represent a generalization of the Birkhoff-Rott equation because the combined kernel* K *can take a more general form. With a generic choice of* K, (2.4) *no longer can be interpreted as a parameterization with respect to circulation and either* (2.4) *or* (2.5) *may be used. In Section 3.2.1, we verify our model by simulating several classical vortex sheet examples. To distinguish our simulations from the direct use of the Birkhoff-Rott equation we use the formulation* (2.5) *and* (2.2) *which yields excellent agreement with* (1.3) *but, in general, either sets of equations can be used.*

3. Numerical method. We implement equations (2.5) and (2.2) using a fourth order Runge Kutta method in time and centered difference discretization for space. In addition, we apply an adaptive mesh method using cubic interpolation for several of the more complicated examples in sections 3.2.1 where more resolution is required. We briefly present this algorithm below.

Let $z = (x, y)$ be the position of the sheet, $v = (u, w)$ be the associated velocity field, and ρ be the density. We denote the associated discretized vectors $z_i = (x_i, y_i)$, $v_i = (u_i, w_i)$ and ρ_i indexed by i. We then have the following discretized equations for (2.2) and (2.5):

$$v_j = \frac{\partial z_j}{\partial t} = \sum_i K(z_j - z_i)\cdot\rho(z_i)|\Delta z_i| \tag{3.1}$$

$$\frac{\partial \rho_j}{\partial t} = -\rho_j\frac{(x_{j+1}-x_{j-1})(u_{j+1}-u_{j-1}) + (y_{j+1}-y_{j-1})(w_{j+1}-w_{j-1})}{(x_{j+1}-x_{j-1})^2 + (y_{j+1}-y_{j-1})^2} \tag{3.2}$$

where

$$|\Delta z_j| = \frac{\sqrt{(x_{j+1}-x_j)^2 + (y_{j+1}-y_j)^2} + \sqrt{(x_j - x_{j-1})^2 + (y_j - y_{j-1})^2}}{2}. \tag{3.3}$$

Furthermore, let F_1, F_2 be vectors defined with the following elements:

$$F_{1,j}(\rho, z, v) = \frac{dz_j}{dt} = \sum_i K(z_j - z_i)\cdot\rho(z_i)|\Delta z_i| \tag{3.4}$$

$$F_{2,j}(\rho, z) = -\rho_j\frac{(x_{j+1}-x_{j-1})(u_{j+1}-u_{j-1})) + (y_{j+1}-y_{j-1})(w_{j+1}-w_{j-1})}{(x_{j+1}-x_{j-1})^2 + (y_{j+1}-y_{j-1})^2} \tag{3.5}$$

Then our Runge Kutta algorithm for one time step is described below.

(a)	$V_1^n = F_1(\rho^n, z^n)$,	$P_1^n = F_2(\rho^n, z^n, V_1^n)$
(b)	$V_2^n = F_1(\rho^n + \Delta t P_1^n/2, z^n + \Delta t V_1^n/2)$,	$P_2^n = F_2(\rho^n + \Delta t P_1^n/2, z^n + \Delta t V_1^n/2, V_2^n)$
(c)	$V_3^n = F_1(\rho^n + \Delta t P_2^n/2, z^n + \Delta t V_2^n/2)$,	$P_3^n = F_2(\rho^n + \Delta t P_2^n/2, z^n + \Delta t V_2^n/2, V_3^n)$
(d)	$V_4^n = F_1(\rho^n + \Delta t P_3^n, z^n + \Delta t V_3^n)$,	$P_4^n = F_2(\rho^n + \Delta t P_3^n, z^n + \Delta t V_3^n, V_4^n)$
(e)	$\rho^{n+1} = (P_1^n + 2P_2^n + 2P_3^n + P_4^n)/6$,	$z^{n+1} = (V_1^n + 2V_2^n + 2V_3^n + V_4^n)/6$

After each Runge Kutta step, we update the tolerance in our adaptive mesh by first setting $\epsilon = \min(\text{total length of curve}/N, \epsilon)$. We then consider the distance between consecutive points and if the distance between them is greater than ϵ we add one point between them using cubic interpolation. In the classical vortex sheet examples (Section 3.2.1) and superfluid calculations (Section 4.1), the kernel K is singular, hence we use Krasny's desingularization technique described in more detail in Section 3.2.1.

3.1. Convergence study. To verify the convergence of our method, we use the periodic perturbation example in section 3.2.1 below. Since the exact solution to this example is unknown, we derive the order of convergence by computing successive differences between numerical solutions. We then double the number of points (in time or in space respectively) and then apply equation (3.6) to estimate the convergence rate.

For the convergence in time, let (z_1, ρ_1), (z_2, ρ_2), (z_3, ρ_3) and (z_4, ρ_4) be used to denote the numerical solution for time discretization $M = 10$, 20, 40, 80 respectively, at $T = 0.1$, with $N = 100$. Then the approximate convergence rate can be calculated as follows

$$\text{Conv. rate} \approx \log(||e_i||_2/||e_{i+1}||_2)/\log 2, \tag{3.6}$$

where e_i can be taken as vectors $z_i - z_{i+1}$ or $\rho_i - \rho_{i+1}$.

For the convergence in space, we use the same notations with capital letters (Z_1, P_1), (Z_2, P_2), (Z_3, P_3) and (Z_4, P_4) to denote the solution for space discretization $N = 100$, 200, 400, 800 respectively, at time $T = 0.1$, with $M = 10$. We use formula (3.6) to compute the approximate convergence rate as before, except that e_i is taken to be vectors $Z_i - Z_{i+1}$ or $P_i - P_{i+1}$. We also compute the convergence in space with the effect of cubic interpolation by starting with the same parameter setting, and successively halving the adaptive tolerance ϵ. We obtain solutions (Z_1, P_1), (Z_2, P_2), (Z_3, P_3) and (Z_4, P_4), and then use formula (3.6) to compute the approximate convergence rate. Our results are summarized in table 3.1.

3.2. Verification of method. Here we test the new algorithm on known exact solutions. First, in section 3.2.1 we recompute some examples of vortex sheets in the literature using the new code and show that the resulting solution is identical to previously published results. Second, in section 3.2.2 we compute some collapsing ring examples in the purely aggregating case and compare the results to ODE theory for these special solutions.

3.2.1. Case 1: incompressible vortex sheet examples. In this section we will verify our model by implementing our method to simulate three vortex sheet problems for the 2D Euler equations. This corresponds to setting $N = \frac{1}{2\pi}\log|r|$ and $G = 0$ in equations (1.1) - (1.2). As mentioned previously, the motion of the vortex sheet is governed by the Birkhoff-Rott equation (1.3) and it is well known that (1.3) is ill-posed due to the Kelvin-Helmholtz instability, see [23, 30]. Thus, in order to

TABLE 3.1
convergence rate in time and space.

Convergence in time				
M	$\|\|z_i - z_{i+1}\|\|_2$	conv. rate	$\|\|\rho_i - \rho_{i+1}\|\|_2$	conv. rate
10				
20	6.1748e-07		7.7979e-06	
40	4.6074e-08	3.7444	5.7844e-07	3.7528
80	3.1409e-09	3.8747	3.9661e-08	3.8664
Convergence in space				
N	$\|\|z_i - z_{i+1}\|\|_2$	conv. rate	$\|\|\rho_i - \rho_{i+1}\|\|_2$	conv. rate
100				
200	1.2027e-04		7.2394e-03	
400	2.1006e-05	2.5174	2.0805e-03	1.7989
800	4.3183e-06	2.2823	5.5382e-04	1.9094
Convergence rate for cubic interpolation				
ϵ	$\|\|z_i - z_{i+1}\|\|_2$	conv. rate	$\|\|\rho_i - \rho_{i+1}\|\|_2$	conv. rate
0.06				
0.03	5.9712e-05		1.3776e-03	
0.015	7.3969e-06	3.0130	3.3832e-04	2.0258
0.0075	1.9556e-06	1.9193	7.5105e-05	2.1714

implement our model to simulate equations (1.1) - (1.2) we must desingularize the kernel. Several approaches have been developed to compute the evolution of vortex sheets [1] which address the Kelvin-Helmholtz instability. For our method we use Krasny's [20] direct desingularization of the kernel N,

$$\nabla^{\perp} N_{\delta} = \frac{(z(\Gamma,t) - z(\Gamma',t))^{\perp}}{|z(\Gamma,t) - z(\Gamma',t)|^2 + \delta^2}, \tag{3.7}$$

where δ is a regularization parameter, to compute the examples in this section.

Our first verification simulates the classical elliptically loaded wing example, [21]. The initial Lagrangian parameterization for the elliptically loaded wing is $(x, y) = (2\alpha - 1, 0)$, where $\alpha \in [0, 1]$. The initial distribution of vorticity ρ is set by $\rho = -d\Gamma/\mathrm{d}x$, where $\Gamma = \sqrt{1 - x^2}$ is the circulation of the vortex sheet, as depicted in Figure 3.1.

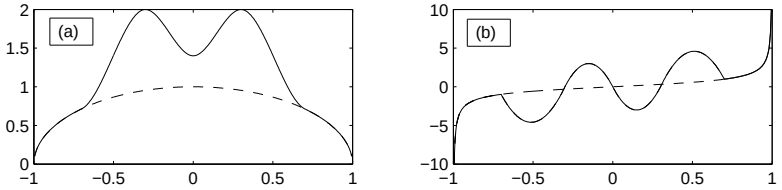

FIG. 3.1. *The initial condition for the elliptically loaded example (dashed line) and the simulated fuselage flap configuration example (solid line). Figure (a) is a plot of the initial circulation against α, and Figure (b) is a plot of the initial density ρ against α.*

Using our adaptive point method with error tolerance $\epsilon = 0.075$, the sheet was initialized using 401 points and at $T = 4$ the number of points grew to 3171. The results are plotted in Figure 3.2 and the observed roll-up is in excellent agreement with Figure 2 in [21].

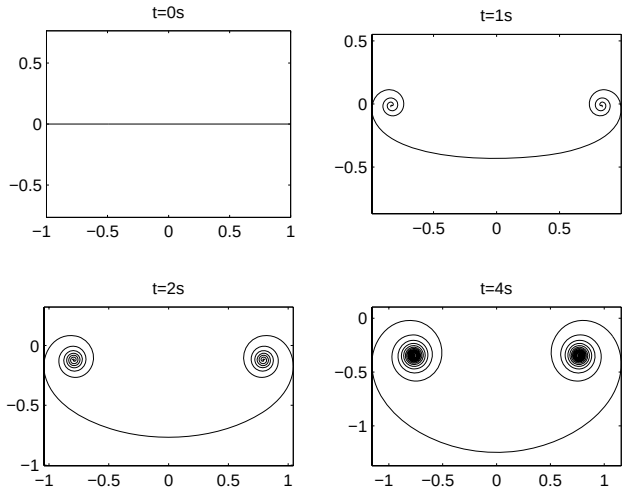

FIG. 3.2. *The numerical solution at $t = 0, 1, 2, 4$ for the elliptically loaded wing example using equations (1.2) and (2.5). We take $\delta = 0.05$, Δt=0.01, and we use adaptive mesh refinement.*

For our second example we apply our model to simulate the more complicated fuselage flap configuration which was first considered in [21]. The initial conditions are chosen to simulate the vorticity generated from a fuselage flap and thus our initial ρ is chosen to be:

$$\rho(\alpha,0) = \begin{cases} x/(1-x^2), & x \in [-1,-0.7] \cup [0.7,1], \\ -3a_3x^2 - 2a_2x - a_1, & x \in [-0.7,-0.3], \\ -3b_3x^2 - 2b_2x - b_1, & x \in [-0.3,0], \\ 3b_3x^2 - 2b_2x + b_1, & x \in [0,-0.3], \\ 3a_3x^2 - 2a_2x + a_1, & x \in [0.3,0.7], \end{cases} \tag{3.8}$$

where a_i and b_i are chosen to ensure continuity.

The initial distribution of both ρ and Γ are plotted in Figure 3.1. We once again initialized our sheet using 401 points and at $T = 4$ the number of nodes grew to the much higher 10151 due to the increased stretching and roll-up as compared to the elliptically loaded wing example. The results are plotted in Figure 3.3 and we once again get excellent agreement with Figure 19 in [23].

In our last example we consider periodic perturbations to a uniformly distributed vortex ring with $\rho = 1$. This example will play an important role in our later studies of both the superfluids and biological examples found in the mixed kernels section (Section 4) so we first present simulations in the purely incompressible case. We focus our attention on perturbations of radially symmetric ring distributions in general because they seem to naturally arise as important solutions in several different contexts, [19, 3]. The spatially periodic perturbation is chosen to be cosine in the normal direction with 10 periods and the magnitude being 1% of the radius. In this example we set the radius to 1 and thus our initial conditions are:

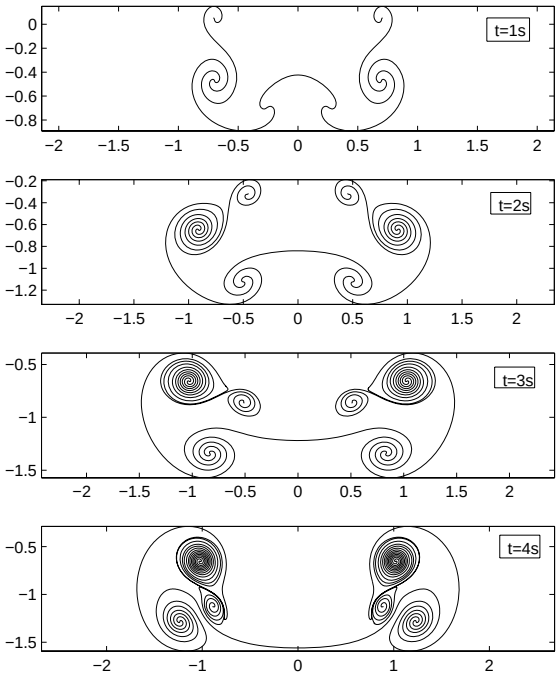

FIG. 3.3. *The numerical solution for the simulated fuselage flap configuration example using equations (1.2) and (2.5). We take* $\delta = 0.1$, Δt*=0.01, and we use adaptive mesh refinement.*

$$r(\alpha) = 1 + 0.01\cos(20\pi\alpha), \qquad \rho(\alpha) = 1 \tag{3.9}$$

$$(x(\alpha), y(\alpha)) = (r(\alpha)\cos(2\pi\alpha), r(\alpha)\sin(2\pi\alpha)). \tag{3.10}$$

We initialize with 400 points and at $T = 4$ the number of nodes has grown to 9670. Figure 3.4 demonstrates several stages of periodic roll-up of the vortex ring.

3.2.2. Case 2: Pure Aggregation. We now turn our attention to a verification of our model when the flow is governed by gradient dynamics, i.e., $N = 0$. For this example we focus on a model exhibiting only aggregation, specifically taking the kernel $K = \nabla G$ where

$$\nabla G = \nabla\sqrt{x^2 + y^2}. \tag{3.11}$$

The active scalar equations with this kernel are well studied, [2, 3, 17, 18]. It was shown in [3] that because the kernel (3.11) does not satisfy the Osgood condition, finite time blow up of radially symmetric solutions occur. In particular, we consider the family of exact solutions of concentric delta rings studied in [3].

To begin, we consider concentric circles (about the origin), with radius r_1, r_2, ..., r_n, and positive initial densities ρ_1, ρ_2,..., ρ_n uniformly distributed over each circle. Because kernel (3.11) is purely attractive and the density is all positive, the predicted behavior is that the rings will contract to the origin under the flow of (1.1) - (1.2).

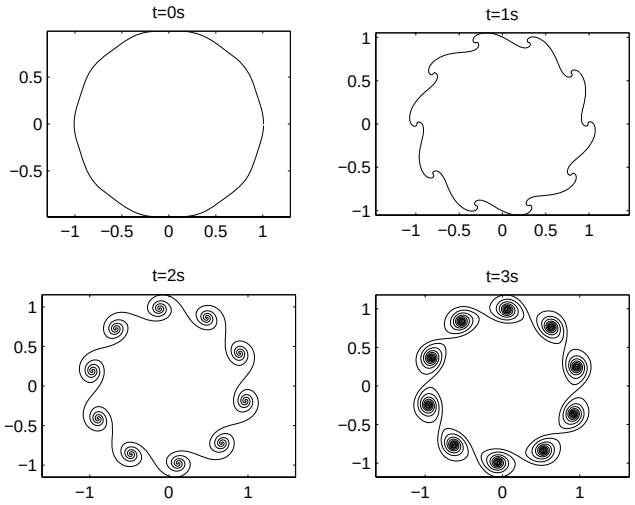

FIG. 3.4. *The numerical solution for the periodic perturbed ring example using equations (1.2) and (2.5). We take* $\delta = 0.05$*,* Δt*=0.01, and we use adaptive mesh refinement.*

TABLE 3.2
ring collapsing time prediction

initial radius	ring clapsing time.					
	One ring case		Two rings case		Three rings case	
method	ODE	Ours	ODE	Ours	ODE	Ours
0.5			0.143	0.144	0.100	0.101
1	0.251	0.251	0.145	0.145	0.101	0.101
1.5					0.103	0.103

In fact, it was shown in [3] that the radius satisfies the following simple ODEs:

$$\frac{\mathrm{d}r_i}{\mathrm{d}t} = -\sum_{j=0}^{n} 2\pi r_j \rho_j \psi(r_i, r_j), \tag{3.12}$$

where

$$\psi(r,\tau) = \frac{1}{\pi}\int_0^{\pi} \frac{r - \tau\cos\theta}{\sqrt{r^2+\tau^2-2r\tau\cos\theta}}\mathrm{d}\theta. \tag{3.13}$$

Thus, to test our method in purely gradient dynamics, we separately simulate our model (2.4) and (2.2) using the kernel (3.11), and then directly solve equations (3.12) - (3.13). We plot the results in Figure 3.5. Figures 3.5a, 3.5c, and 3.5e are the plot of the radius by directly solving (3.12) and (3.13); Figures 3.5b, 3.5d, and 3.5f are the plot of the radius computed using equations (1.2) and (2.5). In each example, all rings have initial density $\rho = 1$. Table 3.2 shows the blow up times for each case and the agreement between our method and the solutions to the ODEs is excellent.

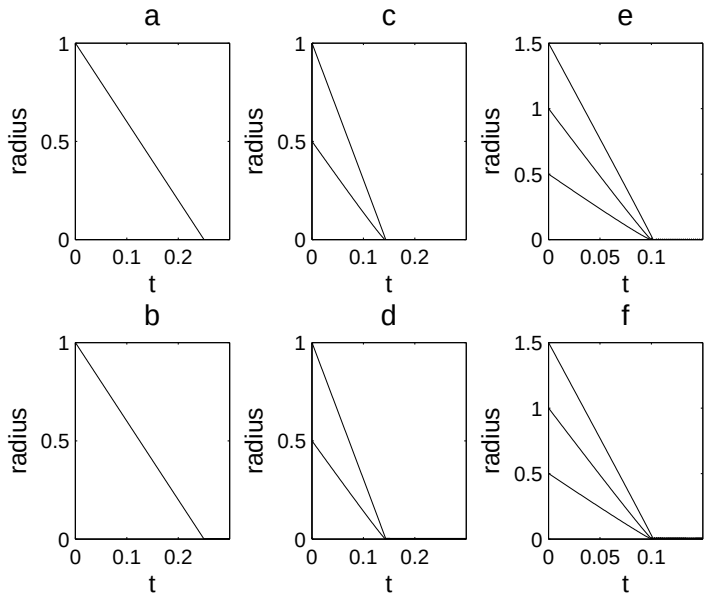

FIG. 3.5. *The comparison of the numerical solution of the radius of rings. In the above 6 pictures, a, c and e are the plot of the radius using equations (3.12) and (3.13); b, d and f are the plot of the radius computed using equations (1.2) and (2.5). a and b are the solutions for the one ring case; c and d are the solutions for the two rings case; e and f are the solutions for the three rings case.*

4. Kernels of mixed type.

4.1. Example 1: Superfluids. We now turn our attention to examples where the kernels are of mixed type. In this section, we consider a family of equations parameterized by θ that arises in the modeling of vortex dynamics for superfluids described in [11]. This family of equations takes the following form:

$$\partial_t \rho + \nabla \cdot (u\rho) = 0, (t, x) \in (0, \infty) \times \mathbb{R}^2 \tag{4.1}$$

$$u = M \nabla \triangle^{-1} \rho, \qquad \rho|_{t=0} = \rho_0 \tag{4.2}$$

where ρ is known as a vortex density function of the superfluid and $M(\theta)$ is a constant orthogonal matrix of the form:

$$M(\theta) = \begin{pmatrix} \cos\theta & -\sin\theta \\ \sin\theta & \cos\theta \end{pmatrix}.$$

This model is derived from the hydrodynamic equations for Ginzburg-Landau vortices [12]. In [11, 24] the authors found that when $\cos\theta = 0$, smooth solutions to (4.1) and (4.2) may blow up in finite time. In addition if ρ_0 changes sign, it was shown that concentration phenomena exist in the approximate solutions sequence of (4.1) and (4.2) regardless of the initial data's degree of regularity. Thus it is interesting to study the vortex sheet problem for (4.1) and (4.2) which is simply a generalization of the classic vortex sheet problem studied in Section 3.2.1.

To match our notation, we may write $\triangle^{-1}\rho = G * \rho$, where $G(r) = -\frac{1}{2\pi} \ln r$ is the fundamental solution of Laplace's equation in $\mathbb{R}^2$. Notice that the parameter θ

controls the contribution to the kernel given by both the incompressible and gradient parts which can be explicitly written out as

$$K(x,y) = K_1(x,y)\cos(\theta) - K_2(x,y)\sin(\theta), \tag{4.3}$$

where $M(\theta)\nabla\triangle^{-1}\rho = K*\rho$ and K_1, and K_2 are defined as $K_1(x,y) = -(x,y)/(2\pi r^2)$ and $K_2(x,y) = (-y,x)/(2\pi r^2)$. Thus if we take $\theta = 0$, $M(\theta)\nabla\triangle^{-1}\rho = K_1 * \rho$ is purely a gradient flow of the Newtonian potential. However, if we take $\theta = -\pi/2$, $M(\theta)\nabla\triangle^{-1}\rho = K_2(x,y) = (-y,x)/(2\pi r^2)$, we recover the Biot-Savart kernel exactly. For the purpose of our study we will consider values of $0 \le \theta \le -\pi/2$ which yield kernels of mixed type (except, of course, the end points). This regime of parameter values ensures the correct sign of the gradient part of the kernel $K_1(x,y)$ is attractive.

We are specifically interested in using our model to better understand the dynamics of vortex density sheets as we vary the parameter θ. From our discussion above it is clear that as θ increases from $\theta = -\pi/2$ to $\theta = 0$ the amount of contribution to our kernel K from the gradient component (attraction) increases while simultaneously the amount of incompressible component (rotation) decreases. What is surprising, though, is that linearly increasing θ has several nonlinear effects on the curve dynamics.

To begin, we use our model to solve for the curve solutions by simply replacing equation (4.1) with (2.5). Since K_1 and K_2 are singular, we use Krasny's desingularization method for both kernels $K_{1\epsilon} = -(x,y)/(2\pi(r^2+\epsilon^2))$ and $K_{2\epsilon} = (-y,x)/(2\pi(r^2+\epsilon^2))$ with $\epsilon = 0.1$. We take perturbations of a vortex ring as our first example with the following initial conditions:

$$(x(\alpha), y(\alpha)) = (r(\alpha)\cos(2\pi\alpha), r(\alpha)\sin(2\pi\alpha)), \qquad \rho(\alpha) = 1, \tag{4.4}$$

where $r(\alpha) = (1 + 0.01\cos(20\pi\alpha))$. We solve equations (2.5) and (4.2) with initial conditions (4.4) for $\theta = -\pi/2$, $-5\pi/12$, $-\pi/3$, $-\pi/4$,$-\pi/6$, $-\pi/12$, and 0, plotting in Figure 4.1 the position of the sheet at $T = 1$.

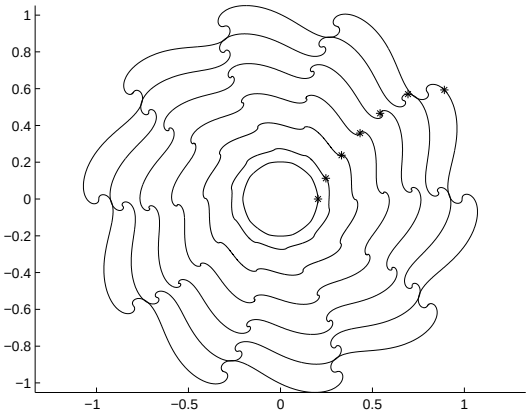

FIG. 4.1. *Plot of the vortex density sheet for several values of θ with initial conditions at T=1. From outside to inside $\theta = -\pi/2$, $-5\pi/12$, $-\pi/3$, $-\pi/4$,$-\pi/6$, $-\pi/12$, and 0. The asterisks represent the point that was initially positioned at $(1,0)$.*

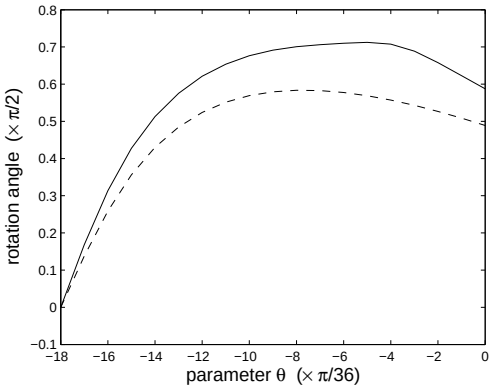

FIG. 4.2. *Plot of the rotation angles at $t = 1$ with respect to parameter θ. The solid curve corresponds to the initial condition of a perturbed ring. The dashed curve corresponds to an initial condition of an unperturbed ring.*

If we record the angle of the asterisks in Figure 4.1 to the horizontal axis we can use this to measure the amount of angular rotation of the ring. The innermost curve corresponds to $\theta = 0$, which is the pure gradient case for the kernel, and the curve clearly exhibits no rotation. The outermost curve corresponds to $\theta = -\pi/2$, which is the purely incompressible case for the kernel; we measure the rotation angle to be approximately 0.187π. One may expect that as we move from the outermost to the innermost curve (increasing θ by $\pi/12$ between any of the two consecutive curves) we should observe a monotonic decrease in rotation angle. Instead, Figure 4.1 shows that the amount of rotation actually increases initially (and peaks near $\theta = -\pi/3$), before eventually decreasing to zero.

We separately plot this rotation angle at $T = 1$ as a function of θ for both the perturbed ring (4.4), and an unperturbed ring in Figure 4.2, seeing that in both cases a maxima occurs on the interior of this range of θ. The maximum angle for the perturbed case is 0.7123, attained at $\theta \approx -14/36\pi$; while the maximum angle for the unperturbed case is 0.5835, attained at $\theta \approx -11/36\pi$. In general, the value of θ for which the maximum angle of rotation occurs is time-dependent but for $t \gg 0$ we observe that a maximum is always found in the interior of $(-\pi/2, 0)$. For t sufficiently small, the maximum angle occurs at the parameter $\theta = -\pi/2$, corresponding to a purely incompressible kernel. Hence, the incompressible kernel dominates the initial rotation dynamics but for slightly longer times the aggregation term plays an important role.

The second aspect of the curve dynamics we would like to study as we vary θ is the amount of roll-up that occurs as a result of the perturbation to the ring. We are also interested in the amplification in time of the perturbation as measured from the unperturbed ring as we vary θ. To study these aspects we selected $\theta = -\pi/2$, $-5\pi/12$, $-\pi/3$ and $-\pi/4$, and plotted the position of the curve at the later time $t = 1.5$ in Figure 4.3. Noting the initial position (marked by an asterisk), it becomes clear that the solutions with $\theta = -\pi/3$ and $-\pi/4$ rotate more than $\theta = -\pi/2$. In addition, we can see in Figure 4.3 that the amplitude of the perturbation also decreases as θ decreases from $\theta = -\pi/2$ to $\theta = -\pi/4$. The amount of roll-up appears to decrease, but unfortunately it is difficult to see in Figure 4.3 due to the smaller amplitude. To

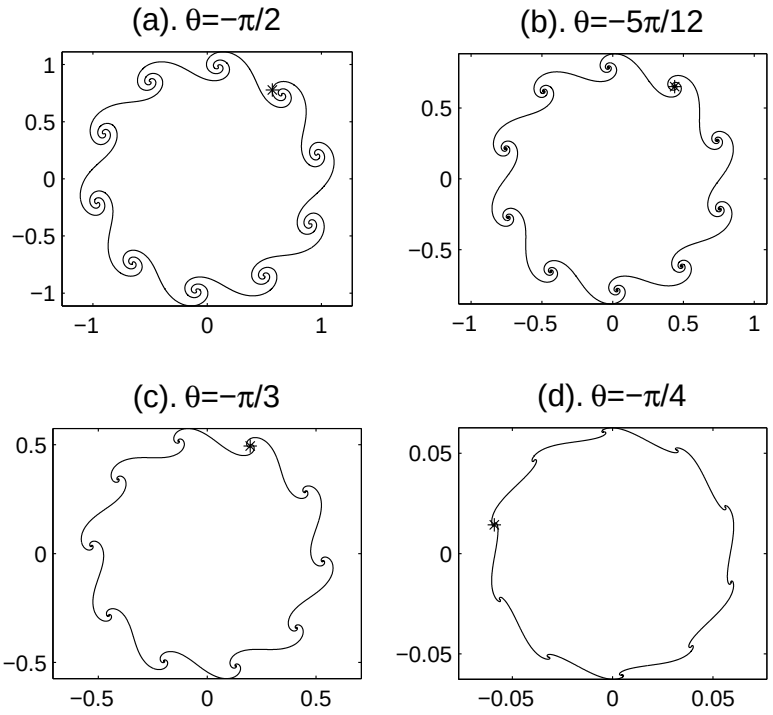

FIG. 4.3. *The solution at time t=1.5 for four different values of θ. The asterisk indicates the position of the point initialized at* $(1, 0)$.

better investigate this phenomenon we focus on one of the roll-ups shown in Figure 4.4 (d). In fact, there are many roll-ups seen by zooming in and careful numerical

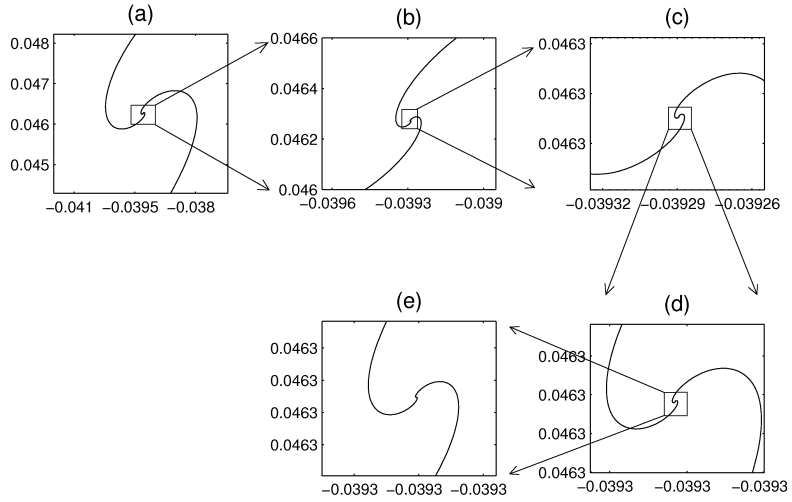

FIG. 4.4. *Subsequent enlargements of a particular roll-up in picture (d) from Figure 4.3. We use 12530 grid points, but the roll-ups structure does not change when we halve the error tolerance, resulting in 25060 points.*

TABLE 4.1
table of wind up numbers

parameter θ	$-\pi/2$	$-5\pi/12$	$-\pi/3$	$-\pi/4$
wind up number	1.5	2.45	2.92	2.47

refinement of the calculation. In order to calculate the wind up numbers precisely, we calculate the tangential angle ϕ at each point numerically using the following formula:

$$\phi_i = \arctan\left(\frac{y_{i+1} - y_{i-1}}{x_{i+1} - x_{i-1}}\right). \tag{4.5}$$

Based on this, we calculate the absolute value of the increase of ϕ by

$$\mathrm{d}\phi_i = |\phi_{i+1} - \phi_i|. \tag{4.6}$$

In one period, the roll-up rotates first counterclockwise and then clockwise an identical amount. Thus, since the perturbation has ten periods, we define the wind up number as $\sum_i \mathrm{d}\phi_i/20$. As seen in Table 4.1, the amount of roll-up actually *increases* with θ, eventually peaking at around $\theta = -\pi/3$ where there are approximately 2.92 rounds of roll-up. The amount of roll-up then begins to decrease. At $\theta = -\pi/4$, which represents an equal amount of incompressible part and gradient part for the kernel, there are only 2.47 rounds of roll-up in the picture.

Thus, we find that both the maximum amount of rotation of the vortex density ring and the amount of roll-up is not a monotone function of θ. For a fixed time $t > 0$ these maxima occur when there is a fully-mixed kernel; i.e., a contribution from both the gradient part and the incompressible part.The amplitude of the perturbation monotonically decreases as θ increases from $\theta = -\pi/2$ to $\theta = 0$. Ultimately, as θ increases and the gradient flow (the attraction) becomes the dominant contributor to the velocity field, both the roll-up and the rotation are damped out.

To explain this behavior physically and mathematically, we consider the linear stability analysis associated with the Kelvin-Helmholtz instability for this more general problem of a fully-mixed kernel. Specifically, we study the linear stability theory of perturbations of a flat constant solution on a periodic domain. Recall that the linear stability analysis of the classic vortex sheet problem [23] demonstrates that the kth Fourier mode grows like $e^{|k|t/2}$ which implies that the linear evolution problem is linearly ill-posed. This ill-posedness explains the rapid development of the complicated roll-up behavior seen in section 3.2.1, classically known as the Kelvin-Helmholtz instability. Following the calculations in [23] we choose the flat vortex density solution to perform this calculation.

Our initial conditions for the flat density sheet problem can be expressed as $z(\alpha, 0) = \alpha + \eta(\alpha, 0)$ with $\alpha \in [-\infty, \infty]$, where $\eta = \eta_2 + \eta_1 i$ is a small perturbation to the position of the sheet. By choosing $\rho|z_\alpha| = 1$ over a fixed period, it is clear that η also represents a perturbation of the density which takes the form $\rho = 1 - \eta_2' + O(\eta_1'^2) + O(\eta_2'^2)$. η_1 represents a perturbation which is perpendicular to the flat sheet. η_2 is a parallel perturbation and is the leading order contribution to the density perturbation. Figure 4.5 shows the evolution of the curve at $t = 1$ for several different values of θ where η_1 is a small Fourier mode 1 perturbation and $\eta_2 = 0$.

We observe all the same phenomena that we saw in the ring perturbation calculation: As θ increases from $-\pi/2$ to $-\pi/4$, the number of roll-ups first increase and then decrease. Second, the roll-ups become smaller and smaller in structure as the

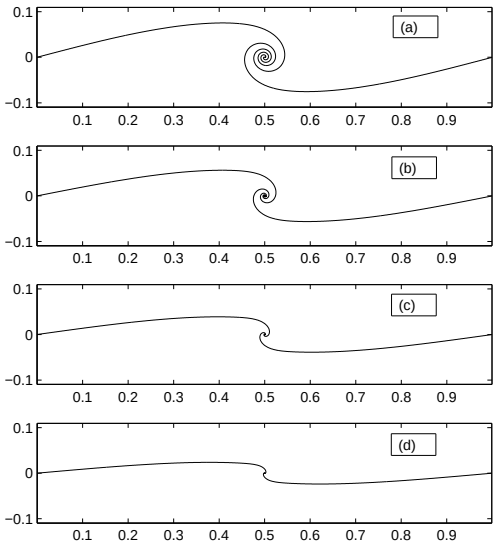

FIG. 4.5. *The solution to the periodic line problem at time $t = 1$, with initial condition $\epsilon \sin(2\pi\alpha)$. (a). $\theta = -\pi/2$, wind up number= 2.64; (b). $\theta = -5\pi/12$, wind up number= 5.04; (c). $\theta = -\pi/3$, wind up number= 4.12; (d). $\theta = -\pi/4$, wind up number= 1.60.*

amplitude of the perturbation (measured from the flat line) lowers as θ increases.

For our stability calculation we use the $K(x, y) = \lambda_1 K_1(x, y) + \lambda_2 K_2(x, y)$, where $\lambda_1 = \cos(\theta)$ and $\lambda_2 = -\sin(\theta)$. By equation (2.5) it is sufficient to understand the linearized evolution equation for $z(\alpha, t)$ which has the form

$$\partial_t \bar{z}(\alpha, t) = \frac{\lambda_2 - \lambda_1 i}{2\pi i} PV \int \frac{d\alpha'}{z(\alpha, t) - z(\alpha', t)}. \tag{4.7}$$

By linearizing around our flat sheet $z(\alpha, t) = \alpha + \eta(\alpha, t)$, we get the following equation

$$\frac{\partial \bar{\eta}}{\partial t} = \frac{\lambda_2 - \lambda_1 i}{2} \mathcal{H}\eta' \tag{4.8}$$

where $\mathcal{H}\eta'$ is the Hilbert transform of η', where η' is the derivative of η with respect to the parameterization and $\bar{\eta}$ is the complex conjugate of η.

REMARK 4.1. *Note that if $\lambda_1 = 0$ and $\lambda_2 = 1$ then equation* (4.8) *recovers the classical Kelvin-Helmholtz instability calculation. Thus, the inclusion of a gradient term can be seen directly in the $-\lambda_1 i$ term in* (4.8).

Letting $\eta(\alpha, t) = A_k(t) e^{i2\pi k\alpha} + B_k(t) e^{-i2\pi k\alpha}$, we get the following relations

$$A_k' = (\lambda_1 - \lambda_2 i)\pi k \bar{B}_k, \qquad B_k' = (\lambda_1 - \lambda_2 i)\pi k \bar{A}_k, \tag{4.9}$$

which yield solutions of the form:

$$A_k(t) = A_k^+ e^{\pi k t} + A_k^- e^{-\pi k t}, \qquad B_k(t) = B_k^+ e^{\pi k t} + B_k^- e^{-\pi k t}. \tag{4.10}$$

We now select an initial condition for our perturbation that contains both a spatial perturbation to the curve (perpendicular to the flat sheet) and density perturbations

(parallel to the flat sheet in the x direction). If we choose $\eta(\alpha,0) = \epsilon_1 i \sin 2\pi m_1\alpha + \epsilon_2 \sin 2\pi m_2\alpha$ then for $k \neq m_1$ or m_2 we get $A_k(t) = B_k(t) = 0$. Otherwise,

$$A^+_{m_1} = \frac{\epsilon_1}{4}(1-\lambda_1+\lambda_2 i), \qquad A^-_{m_1} = \frac{\epsilon_1}{4}(1+\lambda_1-\lambda_2 i), \tag{4.11}$$

$$B^+_{m_1} = \frac{\epsilon_1}{4}(-1+\lambda_1-\lambda_2 i), \qquad B^-_{m_1} = \frac{\epsilon_1}{4}(-1-\lambda_1+\lambda_2 i), \tag{4.12}$$

$$A^+_{m_2} = -\frac{i\epsilon_2}{4}(1-\lambda_1+\lambda_2 i), \qquad A^-_{m_2} = -\frac{i\epsilon_2}{4}(1+\lambda_1-\lambda_2 i), \tag{4.13}$$

$$B^+_{m_2} = -\frac{i\epsilon_2}{4}(-1+\lambda_1-\lambda_2 i), \qquad B^-_{m_2} = -\frac{i\epsilon_2}{4}(-1-\lambda_1+\lambda_2 i). \tag{4.14}$$

The solution to the linearized problem is then: $\eta(\alpha,t) =$

$$\begin{aligned} &i[\epsilon_1(\sin 2\pi m_1\alpha\cosh(\pi m_1 t) - \lambda_1 \sin 2\pi m_1\alpha \sinh(\pi m_1 t)) + \epsilon_2\lambda_2 \sin 2\pi m_2\alpha \sinh(\pi m_2 t)] \\ &+\epsilon_2(\sin 2\pi m_2\alpha\cosh(\pi m_2 t) - \lambda_1 \sin 2\pi m_2\alpha \sinh(\pi m_2 t)) - \epsilon_1\lambda_2 \sin 2\pi m_1\alpha \sinh(\pi m_1 t). \end{aligned} \tag{4.15}$$

From equation (4.15), we can now explain the effect of including a gradient term on the dynamics of the flat vortex density sheet and the Kelvin-Helmholtz instability. If we first consider purely perpendicular perturbations to the vortex density sheet (corresponding to $\epsilon_2 = 0$), our calculation above yields that the kth Fourier mode grows like $e^{|k|t/2}$. This implies that the linear evolution problem is still linearly ill-posed in the fully-mixed case. Hence, just as in the classical Kelvin-Helmholtz instability, we expect a singularity in the curvature of our solution in finite time. The linearization calculation provides the mechanism for the dampened amplitude that we see in the nonlinear calculations in Figure 4.5.

When θ is a bit greater than $-\pi/2$, λ_1 is a small positive number. We can see from equation (4.15) that this is the direct cause of the dampening out of the growth in the y direction. This is observed in Figure 4.5 and is explicitly exhibited in the linearized solutions plot in Figure 4.6 for various θ values. We can now also argue why we observe more roll-up in fully-mixed kernels as opposed to just incompressible motion. At the point of a roll-up, the dampened amplitude along with the added attractive behavior of the gradient kernel forces the vorticity to remain closer together and aggregate at the roll-up point. Thus, by having more "mass" in a closer proximity, the rotational rate of r^{-1} causes this aggregated mass to rotate quicker than if no gradient dynamics were included.

We can also understand from equation (4.15) the linearized dynamics of a pure density perturbation to the curve which corresponds to $\epsilon_1 = 0$. The linearized solution also predicts that the kth Fourier mode in the density grows like $e^{|k|t/2}$, implying that the linear evolution problem is also linearly ill-posed. Another effect of including a gradient term is thus the growth of singularities *in the density* in addition to the singularities in the curvature. In general, an arbitrary small perturbation to the vortex density sheet will generate singularities in both the curvature and the density; an example of this phenomenon is plotted in Figure 4.7. In this example, it appears that the curvature and density singularities occur at the same spatial point. Whether curvature singularities and density singularities must occur at the same place and time is unknown and is an interesting open question.

4.1.1. Biological swarming. We conclude this section by turning our attention from vortex density sheets to a biological model for swarming. In [31], Topaz and Bertozzi study the continuum model (1.1) and (1.2), with the Gaussian kernel

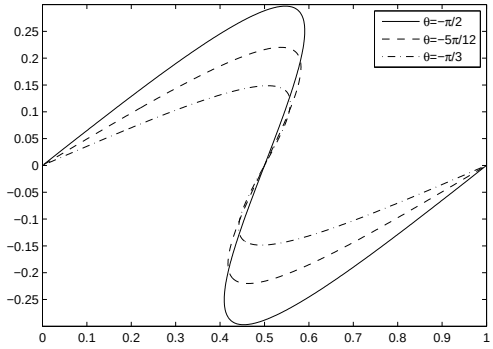

FIG. 4.6. *The solution to the linearized problem at time* $t = 1.3$ *with initial condition* $\epsilon_1 \sin(2\pi\alpha)$. *The solid curve is for* $\theta = -\pi/2$; *the dashed curve is for* $\theta = -5\pi/12$; *the dotted-dashed curve is for* $\theta = -\pi/3$.

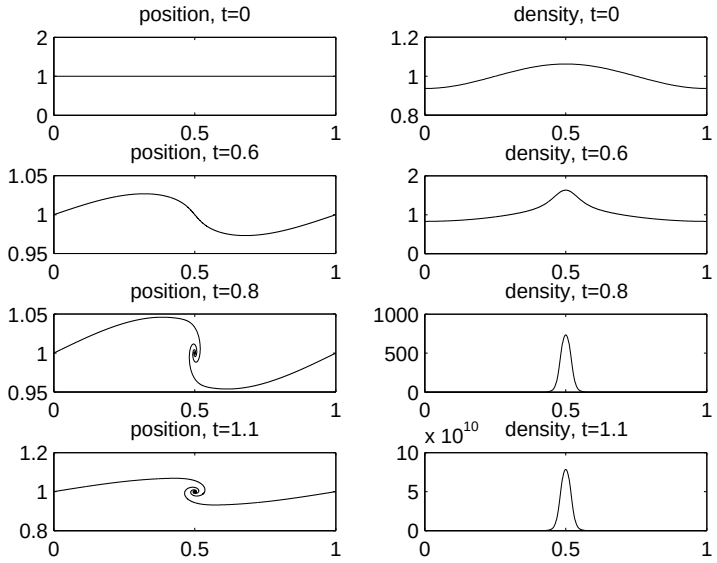

FIG. 4.7. *Time evolution of both the curve and density with* $\eta(\alpha, 0) = 0.01 \sin(2\pi\alpha)$ *with* $\theta = -5\pi/12$. *This pure density perturbation leads to both a curvature and density singularity formation.*

$G_d(x, y) = \frac{1}{d^2} e^{-(x^2+y^2)/d^2}$. The parameter d is the relevant length scale and G_d is used as a biological kernel to model swarming and milling behavior for both incompressible motion N and gradient motion G. They considered localized continuous distributions of the density but ultimately study the dynamics of the incompressible motion and the gradient motion separately. Using our model, we study the dynamics of curve solutions with a fully-mixed kernel of the form $K = \lambda_1 \nabla G_d + \lambda_2^{\perp} \nabla G_d$ where λ_1 is a weight for the gradient contribution to the kernel and λ_2 is a weight for the incompressible contribution to the kernel. Using the same approach as the superflu-

ids example, we would like to understand how incompressible motion and gradient motion affect each other by controlling the weights λ_1 and λ_2 for each.

We study the initial value problem (1.1) and (1.2) using a perturbed density ring with initial conditions of the form (4.4), where

$$r(\alpha) = \bar{r} + \tilde{r}\cos 12\pi\alpha \text{ with } \alpha \in [0,1]. \tag{4.16}$$

For our first two experiments we take $d = 3$ for both G_d in the kernel, and choose $\bar{r} = 1$, with the very large perturbation of $\tilde{r} = 0.2$. We fix the weight of the gradient part in our first simulation to be $\lambda_1 = 1$, and vary the amount of the incompressible part from $\lambda_2 = 0$ to $\lambda_2 = 9$, plotting the solution curves at $t = 50$ in Figure 4.8. By

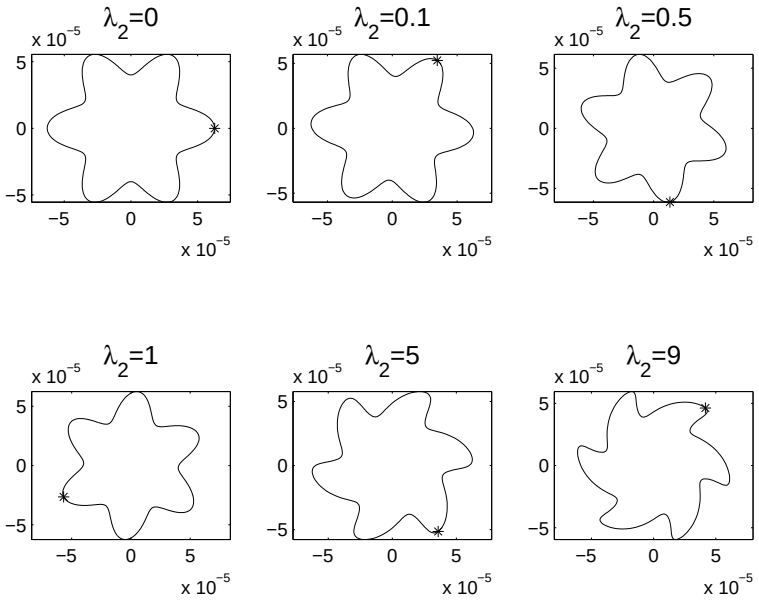

FIG. 4.8. *The solution at time t=50 for $\lambda_1 = 1$ and varying values of λ_2.*

keeping $\lambda_1 = 1$ fixed we can observe how changing the value of λ_2 (the incompressible motion) affects the dynamics with a fixed rate of contraction. From Figure 4.8 it is clear that the amount of rotational shear that occurs on the "spiral arms" increases as λ_2 increases, as one would expect. It is also easy to see that the rate of contraction (using the magnitude of the scale of the curves 5×10^{-5}) is identical regardless of how much incompressible part is added to the kernel. This is also consistent with the superfluids example.

Next, we fix the incompressibility coefficient $\lambda_2 = 1$ and vary the gradient coefficient λ_1 to see how the increase of the gradient affects the rotation and shear of the curve solutions. Figure 4.9 gives the solutions for different λ_1's at time $t = 25$. There are several important features to observe in Figure 4.9. First, it is clear from the axis that as λ_1 increases the rate of contraction increases as expected. Second, we note that the rotational shear of the arms decreases and the amount of rotation of the shape increases as λ_1 increases. We calculate the degree of rotation by measuring the angle from the asterisks to the point $(1, 0)$; the values are recorded in Table 4.2. One noticeable change in the angle occurs between $\lambda_1 = 0.1$ to $\lambda_1 = 0.5$, where the

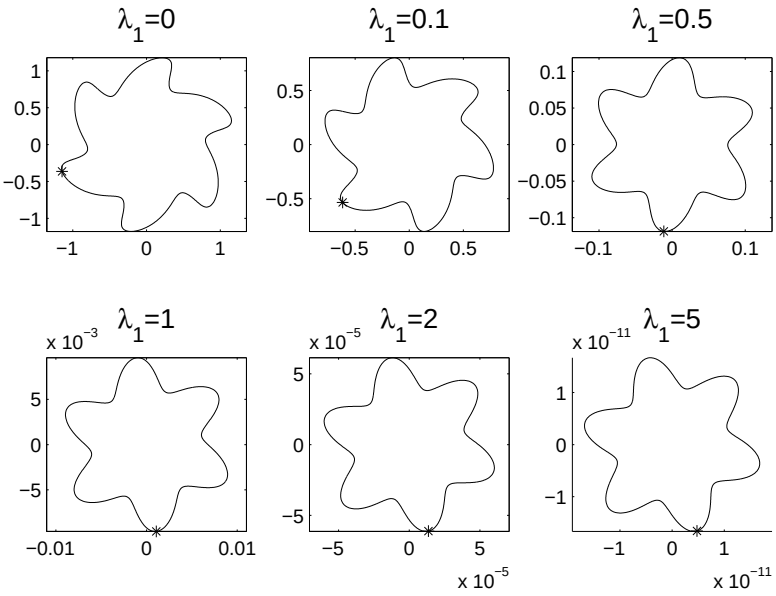

FIG. 4.9. *The solution at time t=25 for* $\lambda_2 = 1$ *and varying values of* λ_1.

angle of rotation changes from 1.23π to 1.47π. Increasing values of λ_1 beyond $\lambda_1 > 1$ yields only small increases in the angle of rotation. Thus, even with a much smoother Gaussian kernel the same theme from the the superfluids example persists: the gradient contribution can have a strong effect on the rotational dynamics but the reverse does not occur.

TABLE 4.2
Table of wind up numbers

Parameter λ_1	0	0.1	0.5	1	2	5
Rotation angle	1.0976	1.2276	1.4700	1.5358	1.5693	1.5894

Perhaps the most interesting behavior we observe in this example is that different spin directions of the perturbation arms occur depending on the relationship between the size of the ring r and the length scale of the kernel d. In our examples $\rho > 0$ the curve thus rotates counterclockwise by the right hand rule. In Figure 4.10(a), which corresponds to $d = 3$ and $r = 1$, the outer arms spin slower in the clockwise direction relative to the curve's speed of rotation, hence the arms appear to be "falling behind." In contrast, Figure 4.10(b) uses the parameters $d = 1$ and $r = 1$, producing a counterclockwise spin of the arms which is faster than the curve's speed of rotation. This forces the arms to "get ahead" of the curve. We can suppose, then, that there must be a critical ratio $\gamma_0 = d/r$ in the behavior of the spiral arms as we increase the parameter d from 1 to 3 where the speeds match.

To estimate γ_0 we first consider the simpler problem of an an unperturbed ring and the velocity ϵ away from the ring depicted in Figure 4.11. Let us assume our initial condition is a circle with radius r and density normalized to $\rho = 1$. For this estimate we will also set $\lambda_1 = 0$ and $\lambda_2 = 1$ in our model to isolate the effect of the

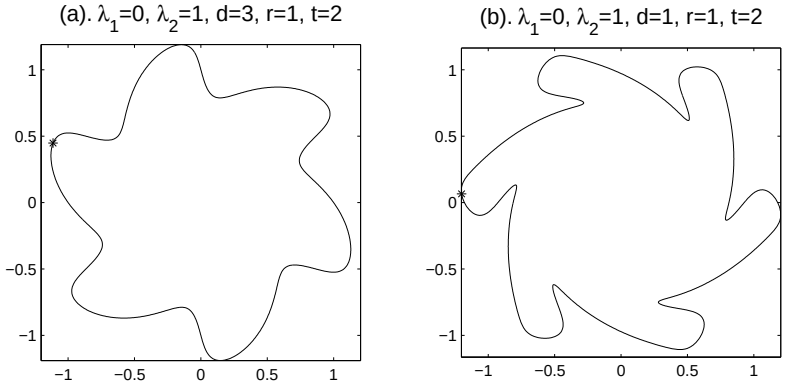

FIG. 4.10. *By choosing parameters d and r, the spin direction of the outer arms are different.*

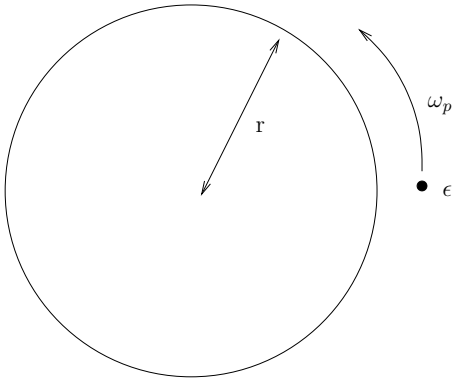

FIG. 4.11. *The initial condition as a circle, with the angular velocity it generates to a point with distance ϵ on the right of the circle.*

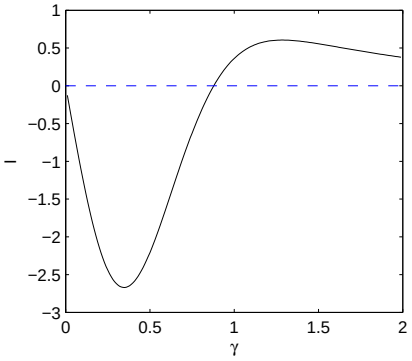

FIG. 4.12. *Integral I as a function of γ. I(0.879)=0.000171 and I(0.878)=-0.003721, indicating that the zero lies between 0.878 and 0.879.*

incompressible velocity field (which is the cause of the rotation rates). This will result in a constant radius r (as opposed to a contracting one), allowing us to pinpoint γ_0 more precisely. We have seen that the amount of gradient in the kernel has an effect on the rotational shearing but we will observe below that the predicted γ_0 seems to be independent of λ_2.

To find the value of γ_0 we need to compute the angular velocity ω_p of a point $p = (1 + \epsilon, 0)$ just outside the ring, i.e., where $\epsilon \ll 1$; see Figure 4.11. This point represents a small radial perturbation of the circle. If this point is moving faster than on the ring then perturbations of the ring will result in spiral arms that shear in the counterclockwise direction relative to the ring, as in example 4.10(b). If the point is moving slower than on the ring the spiral arms will fall behind the ring, as in example 4.10(a). To calculate the angular velocity ω_p of the point p which is a distance ϵ from the circle we compute the integral

$$\omega_p = \frac{1}{r+\epsilon} \int_0^{2\pi} \nabla^\perp G_d(r + \epsilon - r\cos\theta, -r\sin\theta) r \mathrm{d}\theta. \tag{4.17}$$

We then differentiate (4.17) with respect to ϵ and we get to leading order

$$\frac{\mathrm{d}\omega_p}{\mathrm{d}\epsilon} = \frac{2}{d^5} \cdot I, \quad \text{where} \quad I = \int_0^{2\pi} [-\frac{r}{d} 2(1-\sin\theta)^2 + \frac{d}{r}\sin\theta] e^{-2(1-\sin\theta)\frac{r^2}{d^2}} \mathrm{d}\theta. \quad (4.18)$$

We see that the sign of $\frac{\mathrm{d}\omega}{\mathrm{d}\epsilon}$ depends solely on $\gamma = r/d$. When $I < 0$, i.e., $\frac{\mathrm{d}\omega}{\mathrm{d}\epsilon} < 0$, the points on the arm which are closer to the circle have a faster angular velocity. Then the arms appear to wind up in the opposite direction of the spin. When $I > 0$, i.e., $\frac{d\omega}{d\epsilon} > 0$, the points on the arm which are outside the circle have a faster angular velocity, which makes the arms appear to wind up in the same direction as the spin. Thus, our critical value γ_0 is precisely when $I(\gamma_0) = 0$, which is the critical ratio of radius to kernel length scale. Figure 4.12 is a numerical calculation of I as a function of γ. From this we see that $\gamma_0 \approx 0.88$ for our example.

The existence of a critical γ_0 provides the explanation of why we see qualitatively different dynamics in the spiral arms between Figure 4.10(a) and 4.10(b). Since the ratio r/d is what determines the shearing behavior in our simpler problem, we can measure the accuracy of $\gamma_0 = 0.88$ once we include both a nonzero λ_1 and λ_2 in our fully nonlinear perturbation problem. By including a positive value for λ_1 the curve solution will attract toward the origin. Thus, if we start with a ring whose large perturbations initially start outside of the critical radius, we should initially see the arms shear faster than the ring. This faster rotation will cause the arms to move ahead of the ring. However, as the entire curve shrinks and crosses our critical estimate of $\gamma_0 = 0.88$, we would expect the spiral arms to reverse directions. The initial conditions we use for this experiment are described in (4.4) and (4.16), with $d = 1$, $\bar{r} = 1$, and $\tilde{r} = 0.2$. In addition, we take $\lambda_1 = 0.01$ and $\lambda_2 = 0.5$. The plot of the initial condition in Figure 4.13 shows that the large perturbations do in fact lie outside of the critical radius.

As predicted from our calculation, the $t = 3$ plot shows the arms located outside the critical radius moving faster in the counterclockwise direction. However, by $t = 11$ most of the spiral arm has contracted inside the critical radius and begins to reverse course. By $t = 15$ the entire curve and spiral arms are inside the critical radius and the rotational shear becomes pronounced in the reverse direction - shown in Figure 4.13. Thus, our idealized calculation for the critical radius based on the assumption of an unperturbed ring approximates the reversal quite well, though it appears that the reversing of the spiral arm direction in the $t = 11$ picture of Figure 4.13 does occur just outside of the ring.

5. Discussion. In this paper we have derived the evolution equations for the solutions to the general 2D active scalar problem in the case when the active scalar lies on 1D curves. We implement an adaptive Lagrangian scheme which is 2nd order in space and 4th order in time. The model is then shown to reproduce classical vortex sheet dynamics as compared to the desingularized Birkhoff-Rott equation. When the velocity is purely a gradient the model accurately predicts the finite time collapse of power law aggregation equations. When the velocity field contains both an incompressible and gradient component our model exhibits new dynamics which include an increased roll-up associated with the Kelvin-Helmholtz instability for vortex density functions of superfluids. In the second example of mixed type velocity fields we consider a model for biological swarming and aggregation and show that length scale of the kernel plays an important role in the milling and rotational shear behavior of the active scalar curve.

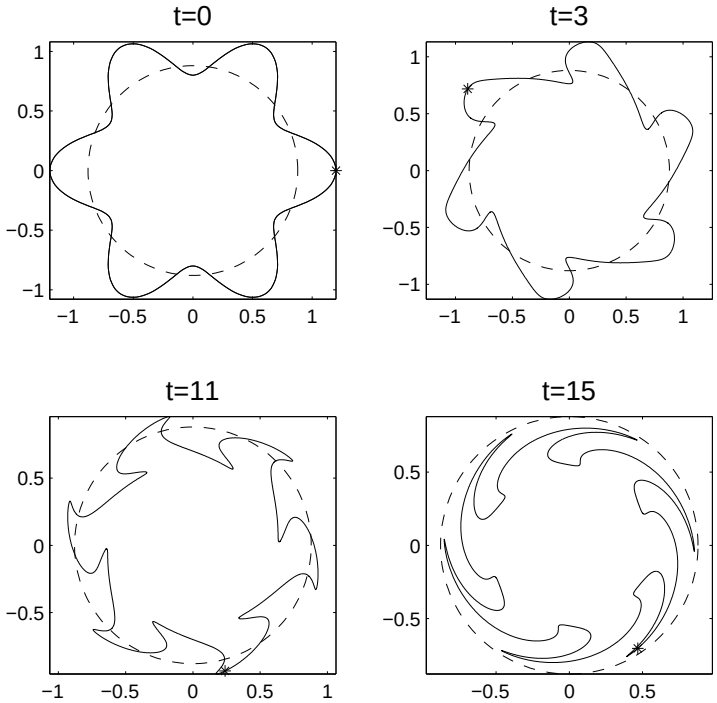

FIG. 4.13. *The solution at time* $t = 0$, 3, 11, 15, *with initial conditions* (4.4) *and* (4.16) *with* $d = 1$, $\bar{r} = 1$, $\tilde{r} = 0.2$, $\lambda_1 = 0.01$, *and* $\lambda_2 = 0.5$

With this new equation there are many future directions of research. As we have seen in these examples, the interaction between gradient and incompressible components provides very rich and nonlinear dynamics. In the superfluids example it would be an interesting physical and mathematical question to better understand the different types of singularity formation (curvature vs. density) and their relation. A second direction of future research is in the area of stability of solutions. Equations (2.5) and (2.2) have already been used to consider both stability of ring solutions and linear well-posedness for attraction-repulsion kernels that are purely a gradient, see [19], and one could extend the analysis to fully-mixed kernels.

REFERENCES

[1] Christopher Anderson and Claude Greengard. On vortex methods. *SIAM J. Numer. Anal.*, 22(3):413–440, 1985.

[2] A. L. Bertozzi and T. Laurent. The behavior of solutions of multidimensional aggregation equations with mildly singular interaction kernels. *Chin. Ann. Math. Ser. B*, 30(5):463–482, 2009.

[3] Andrea L. Bertozzi, José A. Carrillo, and Thomas Laurent. Blow-up in multidimensional aggregation equations with mildly singular interaction kernels. *Nonlinearity*, 22(3):683–710, 2009.

[4] Andrea L. Bertozzi and Thomas Laurent. Finite-time blow-up of solutions of an aggregation equation in $\mathbf{R}^n$. *Comm. Math. Phys.*, 274(3):717–735, 2007.

[5] Garrett Birkhoff. Helmholtz and Taylor instability. In *Proc. Sympos. Appl. Math., Vol. XIII*, pages 55–76. American Mathematical Society, Providence, R.I., 1962.

[6] Michael P. Brenner, Peter Constantin, Leo P. Kadanoff, Alain Schenkel, and Shankar C. Venkataramani. Diffusion, attraction and collapse. *Nonlinearity*, 12(4):1071–1098, 1999.

[7] S. J. Chapman, J. Rubinstein, and M. Schatzman. A mean-field model of superconducting vortices. *European J. Appl. Math.*, 7(2):97–111, 1996.
[8] Peter Constantin, Diego Cordoba, and Jiahong Wu. On the critical dissipative quasi-geostrophic equation. *Indiana Univ. Math. J.*, 50(Special Issue):97–107, 2001.
[9] Peter Constantin, Andrew J. Majda, and Esteban Tabak. Formation of strong fronts in the 2-D quasigeostrophic thermal active scalar. *Nonlinearity*, 7(6):1495–1533, 1994.
[10] Peter Constantin and Jiahong Wu. Behavior of solutions of 2D quasi-geostrophic equations. *SIAM J. Math. Anal.*, 30(5):937–948 (electronic), 1999.
[11] Qiang Du and Ping Zhang. Existence of weak solutions to some vortex density models. *SIAM Journal on Mathematical Analysis*, 34(6):1279–1299, 2003.
[12] Weinan E. Dynamics of vortex liquids in Ginzburg-Landau theories with applications to superconductivity. *Phys. Rev. B*, 50(2):1126–1135, Jul 1994.
[13] Jeff D. Eldredge, Tim Colonius, and Anthony Leonard. A vortex particle method for two-dimensional compressible flow. *J. Comput. Phys.*, 179(2):371–399, 2002.
[14] Hualong Feng, Leon Kaganovskiy, and Robert Krasny. Azimuthal instability of a vortex ring computed by a vortex sheet panel method. *Fluid Dyn. Res.*, 41(5):051405, 16, 2009.
[15] Isaac M. Held, Raymond T. Pierrehumbert, Stephen T. Garner, and Kyle L. Swanson. Surface quasi-geostrophic dynamics. *J. Fluid Mech.*, 282:1–20, 1995.
[16] Miguel A. Herrero and Juan J. L. Velázquez. Chemotactic collapse for the Keller-Segel model. *J. Math. Biol.*, 35(2):177–194, 1996.
[17] Yanghong Huang and Andrea L. Bertozzi. Self-similar blowup solutions to an aggregation equation in $\mathbf{R}^n$. *SIAM Journal on Applied Mathematics*, 70(7):2582–2603, 2010.
[18] Yanghong Huang and Andrea L. Bertozzi. Asymptotics of blowup solutions for the aggregation equation. Submitted.
[19] Theodore Kolokolnikov, Hui Sun, David Uminsky, and Andrea L. Bertozzi. A theory of complex patterns arising from 2D particle interactions. Submitted.
[20] Robert Krasny. Desingularization of periodic vortex sheet roll-up. *J. Comput. Phys.*, 65(2):292–313, 1986.
[21] Robert Krasny. Computation of vortex sheet roll-up in the Treffitz plane. *J. Fluid Mech.*, 184:123–155, 1987.
[22] Fanghua Lin and Ping Zhang. On the hydrodynamic limit of Ginzburg-Landau vortices. *Discrete Contin. Dynam. Systems*, 6(1):121–142, 2000.
[23] Andrew J. Majda and Andrea L. Bertozzi. *Vorticity and Incompressible Flow.* Cambridge University Press, 2002.
[24] Nader Masmoudi and Ping Zhang. Global solutions to vortex density equations arising from sup-conductivity. *Ann. Inst. H. Poincaré Anal. Non Linéaire*, 22(4):441–458, 2005.
[25] Julia K. Parrish and Leah Edelstein-Keshet. Complexity, pattern, and evolutionary trade-offs in animal aggregation. *Science*, 284(5411):99–101, 1999.
[26] Wouter-Jan Rappel, Alastair Nicol, Armand Sarkissian, Herbert Levine, and William F. Loomis. Self-organized vortex state in two-dimensional dictyostelium dynamics. *Phys. Rev. Lett.*, 83(6):1247–1250, Aug 1999.
[27] Takashi Sakajo. From generation to chaotic motion of a ring configuration of vortex structures on a sphere. *Theoretical and Computational Fluid Dynamics*, 24:151–156, 2010.
[28] Theodore C. Schneirla. A unique case of circular milling in ants, considered in relation to trail following and the general problem of orientation. American Museum Novitates. 2002.
[29] Jai Sukhatme and Raymond T. Pierrehumbert. Surface quasigeostrophic turbulence: the study of an active scalar. *Chaos*, 12(2):439–450, 2002.
[30] C. Sulem, P.-L. Sulem, C. Bardos, and U. Frisch. Finite time analyticity for the two- and three-dimensional Kelvin-Helmholtz instability. *Comm. Math. Phys.*, 80(4):485–516, 1981.
[31] Chad M. Topaz and Andrea L. Bertozzi. Swarming patterns in a two-dimensional kinematic model for biological groups. *SIAM Journal on Applied Mathematics*, 65(1):152–174, 2004.
[32] J. J. L. Velázquez. Stability of some mechanisms of chemotactic aggregation. *SIAM J. Appl. Math.*, 62(5):1581–1633 (electronic), 2002.